ANALYSIS AND MODELING OF THE WAVEFIELD GENERATED BY EXPLOSIONS AT THE SAN ANDREAS FAULT OBSERVATORY AT DEPTH

Fred Pollitz, Justin L. Rubinstein, and William L. Ellsworth

U. S. Geological Survey

Sponsored by the National Nuclear Security Administration

Award No. DE-AI52-09NA29328
Proposal No. BAA09-69

ABSTRACT

Surface array and deep borehole recordings of chemical explosions in the near-source (0-20 km) region are studied to better understand the radiated wavefield, and in particular the generation of S-waves by explosions. More than 120 explosions have been conducted in the immediate vicinity of the San Andreas Fault Observatory at Depth (SAFOD) between 2002 and 2006 as part of a comprehensive program to determine the crustal structure and precise location of shallow microearthquakes near the deep drill holes at SAFOD. The data set features more than 70 high-quality digital surface and shallow borehole stations within 10 km of SAFOD; extensive observation of the downgoing wavefield by up to 80 3-component geophones deployed at depths of up to 2.7 km in the SAFOD boreholes; and 86 shot points, including 17 shot points located within a few tens of meters of seismic stations, creating an extensive set of reciprocity observations. Shallow crustal earthquakes have also been extensively observed by the recording networks.

We compare these observations with synthetic seismograms generated using published 3-D crustal models for SAFOD to test prevailing hypotheses of S-wave generation. The methods include a combination of basic source characterization (i.e., point sources represented by a moment tensor), imaging of scattering sources, non-linear wave generation associated with the initial shock wave, and non-linear free surface effects. We compute high-frequency synthetic seismograms in 3-D laterally heterogeneous structure using a new approach based on coupled normal modes. Applying the pure path approximation to a suitably smooth representation of the 3D structure and appropriately revising the eigenfrequencies of the normal modes, amounting essentially to a phase shift of each seismic arrival, reduces the non-linearity of the seismogram with respect to structural parameters. Following this, we apply the Born approximation to the remaining smooth structure (accounting for focusing / defocusing and refraction effects) and non-smooth structure, thus accounting for scattering from relatively short-wavelength structure. Limitations of this approach include:

1. A locked mode approximation must be employed (i.e., an artificial boundary at depth is introduced) in order to keep the number of mode branches reasonably bounded.
2. The effects of multiple scattering, which may affect the amplitude of direct-wave arrivals as well as the character of the coda waves, are not accounted for, since non-smooth structure is implemented with a single-scattering formalism

Keeping the limitations in mind, we apply our method to ~ 4 Hz wave propagation using SAFOD borehole seismometers and the Parkfield Array Seismic Observatory (PASO) array (Thurber et al., 2004). Initial modeling using a smooth 3-D model augmented by random structure shows that observed extended coda following the direct *S* arrival are partially explained by scattering from short-wavelength structure. However, additional structure (e.g., sharp lateral or horizontal discontinuities) may be necessary to explain the precise character of observed coda. We note that *P* coda is typically strong and complicates the identification of *S*-wave energy. We employ polarization analysis to guide the identification of *S* waves. Bearing the above in mind, preliminary analysis of 13 chemical shots during the 2006 PASO-TRES experiment suggests that direct *S*, when it can be unambiguously identified, is polarized as dominantly SV energy. This suggests that the chemical explosions transmit an effective vertical-force component in addition to an isotropic component.

OBJECTIVES

The principal objective of the work being undertaken is to better characterize and understand the generation of *S* waves from explosive sources. The amplitudes of *S* waves are commonly used as a discriminant between explosion- and earthquake-generated sources, in that explosion sources primarily produce *P* waves. Thus, characterizing how *S* waves may be generated by explosive sources is critical to improving explosion discrimination criteria. In this project, we focus on *S* waves generated in the near-source region (0-20 km).

Here we explore the generation of *S* waves from explosive sources using a data set consisting of explosion source data from the San Andreas Fault Observatory at Depth (SAFOD) project (Zoback, et al., 2010). These sources were used by the SAFOD project for site characterization and tomographic imaging, but also can be used for studying shear-wave generation and scattering. This dataset consists of over 120 explosions recorded on a large collection of instruments, both short period and broadband instruments at the surface and at depth. Shots were fired in holes of 5 to 100 feet deep, with shot size ranging between 2 and 100 kg. The shots used high-velocity explosives, such that source durations were very short. Additionally, there were multi-level (32- and 80-instrument) arrays installed in the SAFOD Pilot and Main holes at different times, which can be used to monitor the evolution of the wavefield over short distances.

We explore the generation of shear waves in the near-source region from two directions in the work described here. First, we have developed a methodology for synthesizing seismograms that is less computationally expensive than standard methods and simulates the scattered wavefield. Comparing these synthetic seismograms with observed explosion sources and earthquake sources on the myriad instruments we have available will hopefully show whether shear waves are generated in the near-source region and if so, where and how they are generated as well. The second direction with which we study the generation of shear waves is through examination of the Paulsson Geophysical Service Incorporated (PGSI) multi-level instrument array that was deployed directly below explosion sources. Examining amplitudes, arrival times, and polarizations we hope will reveal how, when and where shear waves are generated within 2 km of explosive sources.

RESEARCH ACCOMPLISHED

Methodology for Scattering of High-Frequency Waves

High-frequency seismic waves recorded at the surface are highly scattered. The prolonged nature of the *P* and *S* codas can be explained as the presence of scattered energy (e.g., Aki & Chouet, 1975). In order to study high frequency wave propagation in a heterogeneous crust, we have developed a new method to synthesize high-frequency seismograms using scattering theory in the context of coupled normal modes (e.g., Friederich, 1999). An expedient in applying coupled mode theory is the use of path-dependent reference models, which account to a large extent for the nonlinear dependence of the seismic waveforms with respect to the overall structure (e.g., Meier et al., 1997). This expedient is akin to the Rytov approximation (e.g., Snieder & Lomax, 1996), which accounts for the first-order shift in arrival times of propagating waves arising from a component of structure. The phase shift for a (path-dependent) spherically symmetric perturbation is already known in analytical form in terms of a perturbation to the mode eigenfrequency, and we shall refer to it as the pure-path approximation. The pure-path approximation represents the effect of smooth structure on the full wavefield to first order, and the leading term of our representation of the synthetic wavefield employs this approximation. Application of the Born approximation using the pure-path-approximated full wavefields accounts for scattering from remaining small-scale heterogeneities (as well as smooth heterogeneities which differ from the path average, leading to focusing and defocusing effects).

Figure 1 shows a ‘constant gradient model’ for the SAFOD area that we use as a reference structure, and Figure 2 shows the normal mode dispersion on this model. We illustrate the computational method with an example of scattering from a point heterogeneity. Figure 3 shows the incident and scattered wavefields resulting from an explosive point source placed at 3.5 km depth. The wavefield is shown on various vertical planes that intersect along a vertical line segment which contains the scatterer. The scattered displacement field on the $y = 0$ plane illustrate scattered P→P and P→SV waves that first appear after the incident *P* wave arrives at about 0.57 sec, and that on the $y' = 0$ plane illustrates scattered P→SH waves. The incident wavefields also display reflections of incident *P* off the free surface as well as the artificial boundary at 7 km depth, leading to the propagation of converted *P* and SV waves. The interaction of these reflected waves with the scatterer just begins to develop at the last plotted snapshot at t = 1.2 sec.

Wave Propagation Through the SAFOD Crustal Volume

An extract of the 3-D Zhang et al. (2009) v_p model projected over a 8 × 8 km^2 map area is shown in Figure 4. We use this and their corresponding v_s model, combined with a density- v_p relationship (Brocher, 2005), to derive a 3-D model of lateral variations in density and elastic parameters. (Figure 1 shows the lateral average of this 3-D model.)

We compare synthetic velocity seismograms with observed seismograms for a small shallow earthquake, Md = 1.2, that occurred in 2002 on the San Andreas Fault in the region of maximum horizontal velocity gradient in the model. Figure 5 shows observed and synthetic seismograms filtered at 4 Hz at 26 PASO sites in order of increasing distance from the source. For the synthetics we use either the Born-scattering wavefield (pure path + scattering terms; continuous green traces) or the leading term (pure path term only; dashed red traces) and implement the source as a point horizontal shear dislocation on a N40◦W vertical plane at 3.7 km depth. The arrival times of the *S* waves are roughly matched by the models, though the initial *S* waveform is difficult to match. Comparing the synthetics with pure path + scattering terms (solid green curves) with those involving only the pure path term (dashed red curves), the main effects of scattering are focusing / defocusing and lateral refraction. For example, from the simulations we can see that the *S* wave has undergone focusing at RCKY (i.e., the data has higher amplitude than the simulation) and defocusing (the data has lower amplitude than the simulation) at HOTF and CRAK. The synthetics do not capture the extended coda waves generally observed for ~1 sec after the *S* arrival. This is to be expected from seismic wave propagation through the relatively smooth Zhang et al. (2009) structure, which primarily modifies the phase and amplitude of the arrivals but does not produce significant coda waves.

It is well known that coda following direct *P* and *S* arrivals at relatively high frequencies (> 1 Hz) are produced by scattering from relatively short wavelength structure (Aki, 1969, 1973), and this scattering process also leads to apparent attenuation of the direct arrivals (Aki & Chouet, 1975; Aki, 1980; Wu, 1982). Several studies have implemented short-wavelength structure in terms of a random media with scale lengths of a fraction of a wavelength of the dominant high-frequency waves (e.g., Frankel & Clayton, 1986). As one example, we implement a simple random medium by adding a random component of shear modulus to the original seismic structure. This structure is converted into corresponding perturbations in v_s and v_p assuming that the v_p / v_s ratio equals its original value in each cell. Synthetics using the velocity model with randomized perturbations (not shown) have coda durations matching those observed, but their amplitudes still do not match observations.

Near-field *S*-wave generation is further illuminated by observations of near-surface explosions recorded by SAFOD downhole arrays. Shots conducted during the November 1-2, 2006 virtual earthquake experiment at several PASO stations were recorded by a three-component seismometer in the SAFOD main hole at 2.654 km depth below the surface. Figure 6 shows an observed velocity seismogram from a ~10 m deep chemical shot at KOOL (solid curve) compared with the Born-scattering wavefield. The transverse component contains a moderate amount of energy that cannot be explained by scattering from the smooth Zhang et al. (2009) structure. On the vertical and cylindrical-radial components, the direct arrival (in both observed and synthetic seismograms) is a combination of direct *P* and pP, and the later arrival is pS reflected off the free surface. These arrivals are a common feature of near-surface explosions generated both with and without surface topography (e.g., Xie et al., 2005; He et al., 2008). Figure 7 confirms that these phases are generated by a near-surface explosion with flat topography, imparting downgoing SV energy into the crust. The character of these free-surface reflections is important because they and other phases (e.g., Rg) generated in the near field contribute to Lg wave propagation (e.g., He et al., 2008). Continued work with our approach and other numerical wave-computation approaches can further quantify the effect of near-source scattering, including surface topography. In addition, the near-surface zone is probably more heterogeneous than the deeper zone, enhancing multiple scattering.

Very Near-Source (<3000m) Generation of *S* Waves

The seismometers in the (PGSI) array have proven to be instructive in constraining where *S* waves are generated by small, contained explosions. The PGSI array contains eighty levels, spaced at 15-meter intervals, each with a 3-component 15 Hz seismometer. This pipe-deployed array uses a flexible bladder to hydraulically clamp the seismometer to the steel casing in the well. During deployment of the array 6 small shots (5 to 10 lbs buried 10 to

15 ft below the surface) were fired from a shot point 40 m from the well-head. This permits wave propagation to be tracked for the entire 2700 meters that the array occupied (Figures 8, 9). The upper ~100 intervals are in a near-vertical section of well, with very small offset from the shot-points. Given this source-receiver geometry, we don't expect to see *S* waves radiated in the downward direction, unless symmetry is broken at the shot-point.

Visual examination of the wavefield shows that the *S* waves present in the wavefield recorded on the downhole string are very weak (Figures 8, 9). First, we note that amplitudes on the radial (near vertical component) are much larger than anything on the horizontal components. Since the array is vertical in its upper half and the shot point is at near zero offset, the vertical ground motion should contain only P waves and any *S* should be on the two horizontal components. At the upper ~40 stations, we identify waves traveling at a velocity close to the computed *S* velocity of 1747 m/s (1/√3 times the observed *P* velocities of 3025 m/s) only on the vertical channel (Figure 8a). These *S* waves have a zero-offset intercept of about 0.5s after the origin time. Clearly they cannot be directly radiated by the source and, thus must be converted waves. We cannot clearly identify energy arriving on the horizontal components that has the appropriate moveout for *S* waves radiated by the source. In addition to energy strongly coming in at the computed *P* velocities, we can see clear reflections from the bottom of the well (Figure 8a) and some very late arriving waves with very slow velocities (~350 m/s and ~1500 m/s). These very slow waves appear to be tube waves (White and Lessenger, 1988).

CONCLUSIONS AND RECOMMENDATIONS

Since scattering is a major component of the high-frequency wavefield, it is critical to include it in the generation of high-frequency synthetics. We have explored a new method of synthesizing seismograms based on using coupled normal modes which allows for the simulation of first-order scattering. Using this method at ~4 Hz we generally reproduce the arrival time of the initial *S* arrival, but observed S (and P) arrivals have more complicated waveforms and are typically followed by coda waves. Waveforms and coda duration are difficult to match with a model of wave propagation through a smooth 3D medium. Adding random noise to the velocity model that we use improves the match to the duration of the coda, indicating that much of the *S* waves generated near to explosive sources are generated from scattering. This is further supported from data coming from the PGSI deployment, where there is scant evidence for *S* waves at stations directly below the explosions where there will be less scattered energy. Continuing work will focus on (1) the implementation of other numerical seismic wave propagation algorithms (e.g., finite element), (2) imaging techniques to characterize the sources of scattered energy from PASO array recordings, and (3) source modeling at relatively long period to characterize the amount of non-isotropic energy radiating from the chemical sources.

REFERENCES

Aki, K., (1969). Analysis of seismic coda of local earthquakes as scattered waves, *J. Geophys. Res.* 74: 615–631.

Aki, K., (1973). Scattering of P waves under the Montana LASA, *J. Geophys. Res.* 78: 1334–1346.

Aki, K., (1980). Scattering and attenuation of shear waves in the lithosphere, *J. Geophys. Res.* 85: 6496–6504.

Aki, K. & Chouet, L. B., (1975). Origin of coda waves: Source, attenuation, and scattering effects, *J. Geophys. Res.* 80: 3322–3342.

Friederich, W., (1999). Propagation of seismic shear and surface waves in a laterally heterogeneous mantle by multiple forward scattering, *Geophys. J. Int.* 136: 180–204.

He, Y., Xie, X.-B., and Lay, T., (2008). Explosion-source energy partitioning and Lg-wave excitation: Contributions of free-surface scattering, *Geophys. J. Int.* 98: 778–792.

Meier, T., Lebedev, S., Nolet, G., & Dahlen, F., (1997). Diffraction tomography using multimode surface waves, *J. Geophys. Res.* 102: 8255–8267.

Snieder, R. & Lomax, A., (1996). Wavefield smoothing and the effect of rough velocity perturbations on arrival times and amplitudes, *Geophys. J. Int.* 125: 796–812.

Thurber, C., S. Roecker, H. Zhang, S. Baher, and W. Ellsworth (2004). Fine-scale structure of the San Andreas fault zone and location of the SAFOD target earthquakes, *Geophys. Res. Lett.,* L12S02, doi:10.1029/2003GL019398.

Thurber, C. H., Zhang, H.,Waldhauser, F., Hardebeck, J., Michael, A., & Eberhart-Phillips, D., (2006). Three-dimensional Compressional Wavespeed Model, Earthquake Relocations, and Focal Mechanisms for the Parkfield, California, Region, *Bull. Seismol. Soc. Am.* 96: S38-S49S49, doi: 10.1785/0120050825.

White, J.E. and Lessenger, M.A., (1988), Caliper effect on borehole coupling, *Exploration Geophys.* 19: 201–205.

Wu, R.-S., (1982). Attenuation of short-period seismic waves due to scattering, *Geophys. Res. Lett.* 9: 9–12.

Xie, X.-B., Ge, Z., and Lay, T., (2005). Investigating explosion source energy partitioning and Lg-wave excitation using a finite-difference plus slowness analysis method, *Bull. Seismol. Soc. Am.* 95: 2412–2427.

Zhang, H., Thurber, C., & Bedrosian, P., (2009). Joint inversion for Vp, Vs, and Vp/Vs at SAFOD, Parkfield, California, *Geochem. Geophys. Geosyst.*, 10, Q11002, doi:10.1029/2009GC002709.

Zoback, M., S. Hickman, W. Ellsworth, (2010), Scientific Drilling into the San Andreas Fault Zone (2010), *Eos, Trans. Am. Geophys. Un.,* 91: 197, doi:10.1029/2010EO220001.

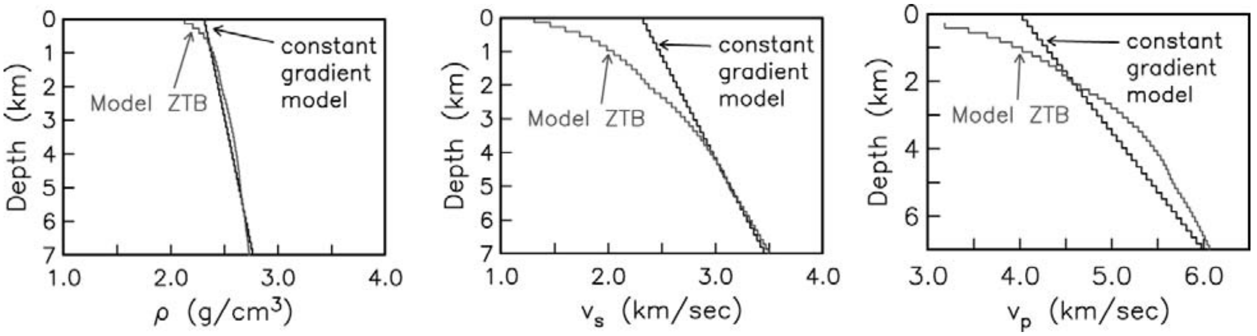

Figure 1. Density and seismic velocities as a function of depth on a synthetic reference model with a constant velocity gradient and the laterally averaged velocities on the Zhang et al. (2009) 3D model of the SAFOD area.

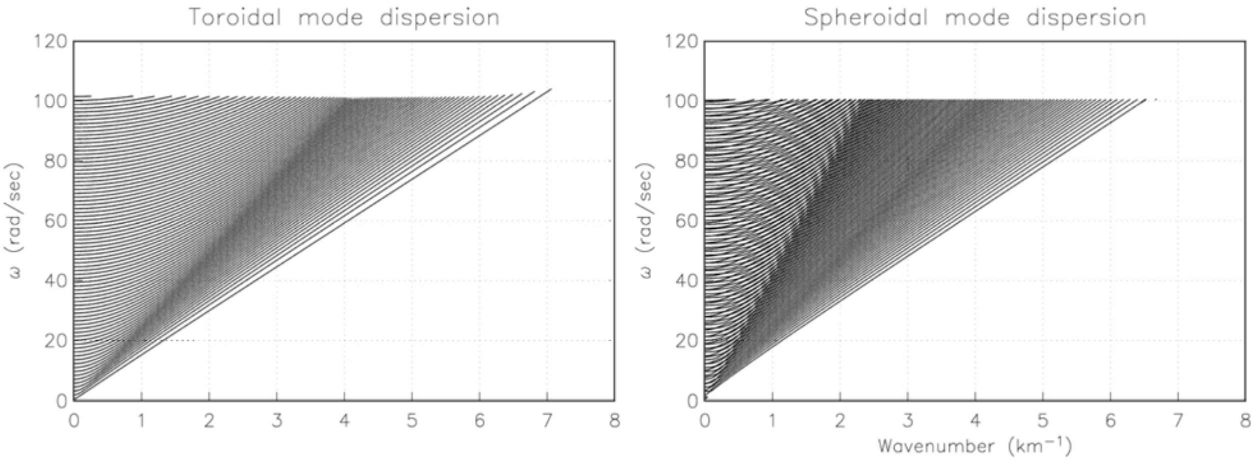

Figure 2. Eigenfrequencies of spheroidal and toroidal modes as a function of wavenumber on the synthetic model shown in Figure F1.

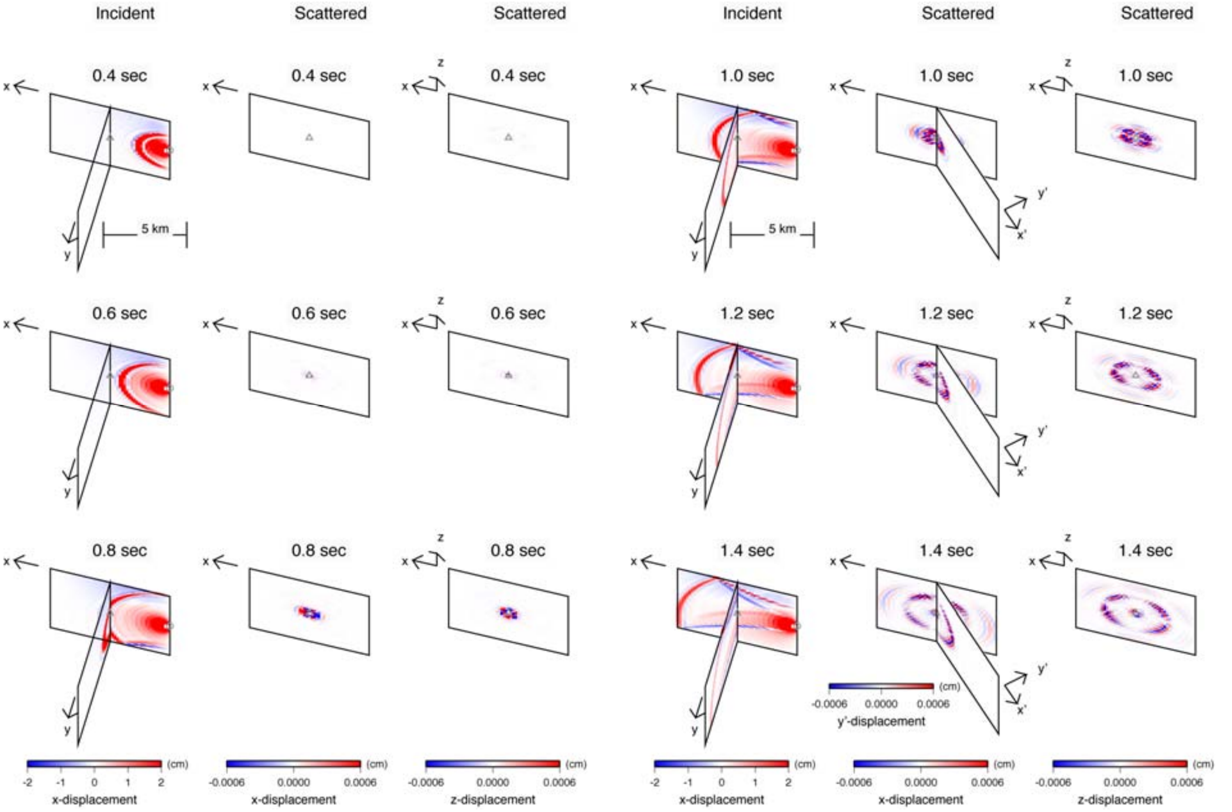

Figure 3. Incident and scattered displacement fields on various vertical sections resulting from an explosive source at depth 3.5 km (gray circle). The incident displacement field interacts with a point scatterer at depth 3.5 km (gray triangle) 4 km from the source. For the incident wavefield, the x− horizontal displacement field is shown on the x = 0 and y = 0 planes. For the scattered wavefield, the x− and z−components are shown on the y = 0 plane, and the transverse component scattered displacement field is shown on the y' = 0 plane, which makes a 45^o angle with each of the other planes. The three planes intersect at a vertical line segment which passes through the scatterer.

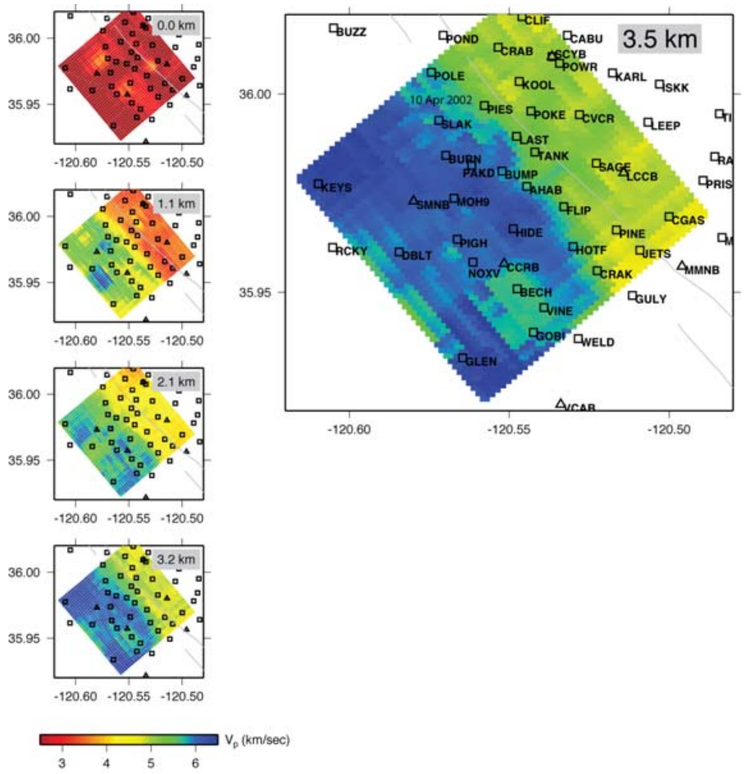

Figure 4. Subset of V_p structure in the SAFOD area (Zhang et al., 2009) on a 3D volume of dimensions 8 × 8 km2 (in map view) ×4.0 km in depth. Squares and triangles denote PASO and HRSN stations, respectively. Location of the M=1.5 10 April 2002 earthquake (depth = 3.5 km) is indicated with text.

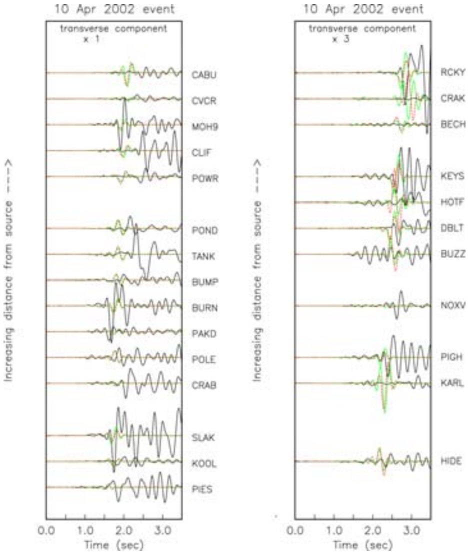

Figure 5. Transverse-component velocity seismograms at PASO stations for the April 10, 2002 event at 3.7 km depth (Thurber et al., 2003) (in black) compared with synthetic velocity seismograms. The synthetics in continuous green are calculated using the 3D Zhang et al. (2009) tomographic model and filtered at 4 Hz. The synthetics in dashed red are calculated using the pure path term only. The observed seismograms are band-pass filtered between 0.2 and 4 Hz. The right column shows more distant stations than the left column – the synthetics in the right column have been multiplied by 3 to help match the recordings.

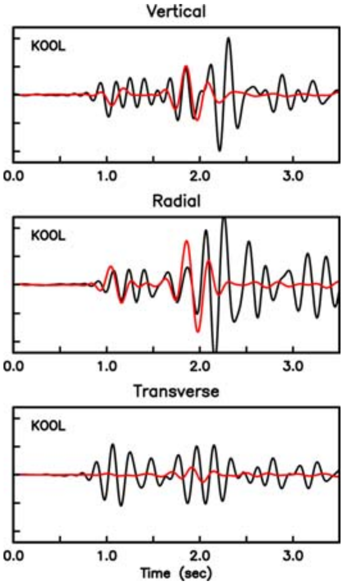

Figure 6. Observed (black) and synthetic (red) seismograms for a surface chemical explosion at KOOL recorded in the SAFOD main hole at depth 2.654 km below the surface.

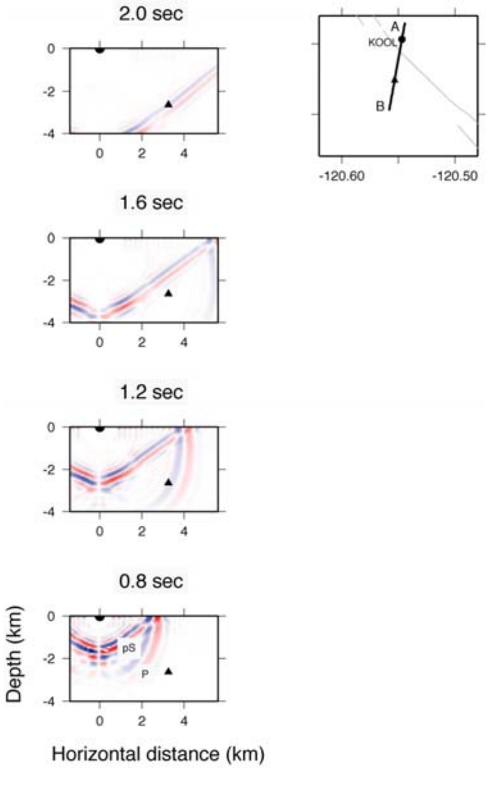

Figure 7. Cylindrical-radial component of synthetic wavefield generated by explosion at 0.01 km depth (indicated by black circle) at the location of PASO site KOOL, indicated by "A". The synthetics are generated with pure path term only in the Zhang et al. (2009) model. The location of the main-hole seismometer is indicated by the black triangle "B". Grey lines indicate faults.

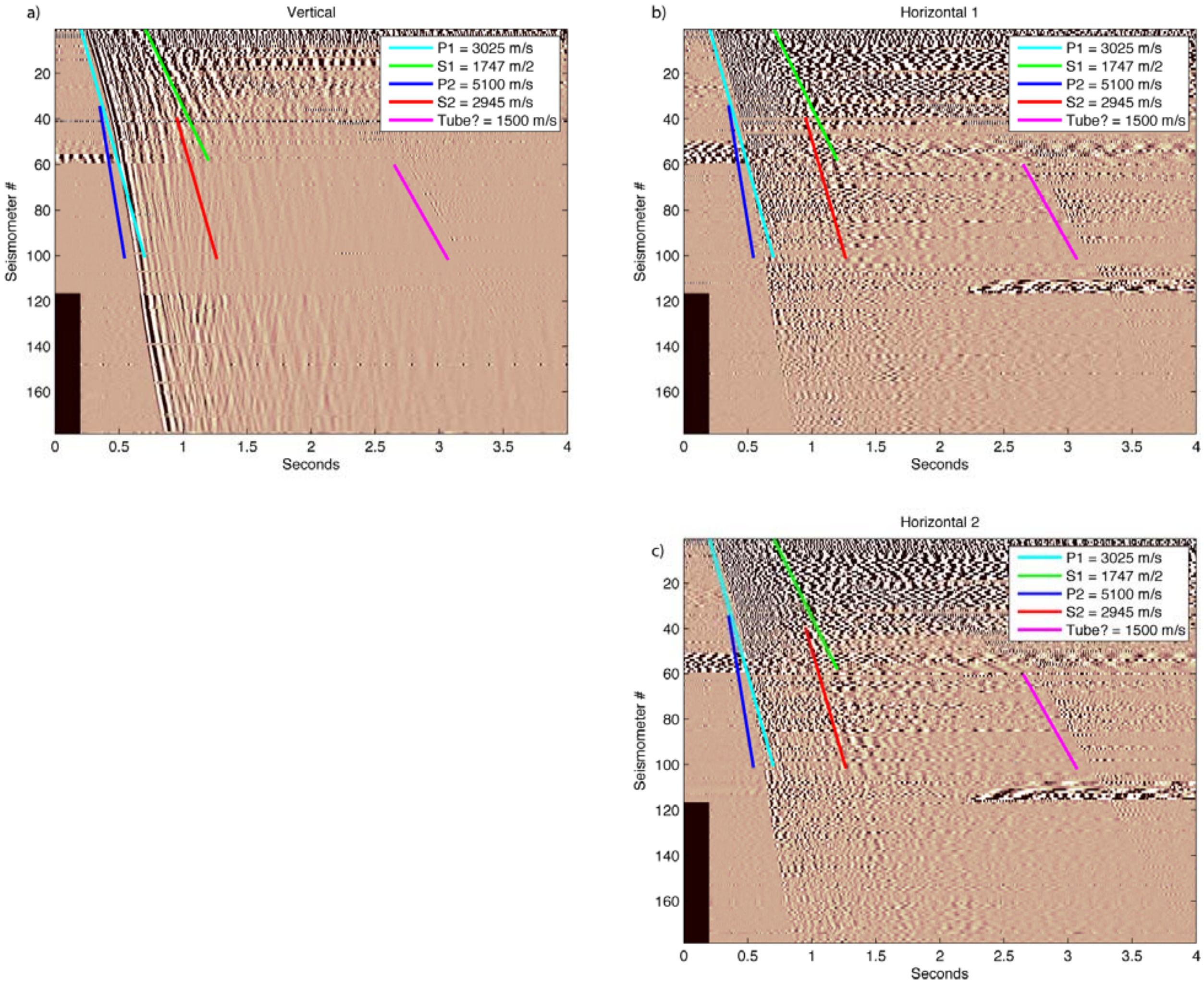

Figure 8: Seismic gathers for the PGSI array spanning the length of the well. Three different shots have been merged so that these records span the well. Amplitudes are all normalized to the same value. The well is near vertical for stations 1-100, where it makes an abrupt turn, thus we cannot interpret across this boundary. Station spacing is 15m, so depth of the sensors can be easily computed. The initial *P* arrival can be clearly identified on the vertical component, and the velocity of this is indicated with cyan and blue lines with the appropriate slope – these are placed before the arrival so that they can be seen. An assumed *S* velocity is also shown for the two observed *P* velocities and is indicated with green and red lines. Arrivals with the upper *S* velocity can be seen on the vertical component, but they arrive more than 0.5 seconds after the *P* arrival. What appears to be a tube wave is also seen much later, as indicated by the magenta line, this can be seen on all components.

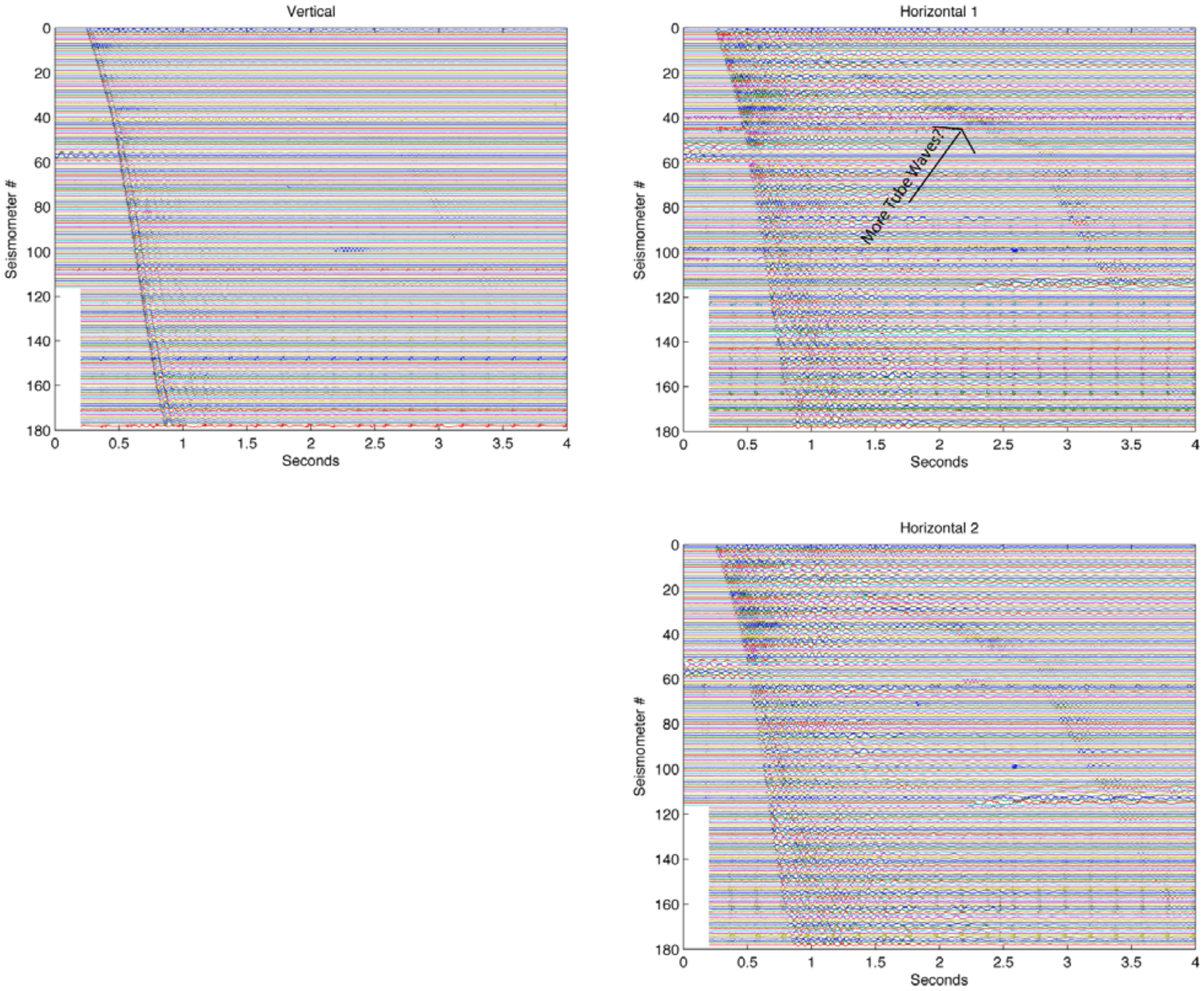

Figure 9: Seismic gather for the PGSI array spanning the length of the well. Amplitudes for each trace are normalized, relative amplitudes from trace to trace are not meaningful. The *P* arrival is very simple and is much larger than anything else on the vertical trace (and even larger than anything on the horizontal components, but due to scaling this cannot be seen here). In addition to the arrivals visible in Figure 8, there is an incredibly slow arriving phase (~350 m/s) that appears to connect to what we believe to be a tube wave at lower depths, this is indicated on the first horizontal component.